A Direct-Bandgap 2D Silver-Bismuth Iodide Double Perovskite: The Structure-Directing Influence of an Oligothiophene Spacer Cation.

Manoj K. Jana,[1] Svenja M. Janke,[1,4] David J. Dirkes,[2] Seyitliyev Dovletgeldi,[3] Chi Liu,[4] Xixi Qin,[1] Kenan Gundogdu,[3] Wei You,[2] Volker Blum,[1,4] and David B. Mitzi[1,4*]

[1]Department of Mechanical Engineering and Materials Science, Duke University, Durham, North Carolina 27708, United States

[2]Department of Chemistry, University of North Carolina at Chapel Hill, Chapel Hill, North Carolina 27599, United States

[3]Department of Physics, North Carolina State University, Raleigh, North Carolina 27695, United States

[4]Department of Chemistry, Duke University, Durham, North Carolina 27708, United States

ABSTRACT: Three-dimensional (3D) hybrid organic-inorganic lead halide perovskites (HOIPs) feature remarkable optoelectronic properties for solar energy conversion but suffer from long-standing issues of environmental stability and lead-toxicity. Associated two-dimensional (2D) analogs are garnering increasing interest due to superior chemical stability, structural diversity and broader property tunability. Towards lead-free 2D HOIPs, double perovskites (DPs) with mixed valent dual metals are attractive. Translation of mixed-metal DPs to iodides, with their prospectively lower bandgaps, represents an important target for semiconducting halide perovskites, but has so far proven inaccessible using traditional spacer cations due to either intrinsic instability or formation of competing non-perovskite phases. Here, we demonstrate the first example of a 2D Ag-Bi iodide DP with a direct bandgap of 2.00(2) eV, templated by a layer of bifunctionalized oligothiophene cations—i.e., (bisaminoethyl) bithiophene—through a collective influence of aromatic interactions, hydrogen bonding, bidentate tethering and structural rigidity. Hybrid density functional theory calculations for the new material reveal a direct band gap, consistent with the experimental value, and relatively flat band edges derived principally from Ag-d/I-p (valence band) and Bi-p/I-p (conduction band) states. This work opens up new avenues for exploring specifically designed organic cations to stabilize otherwise inaccessible 2D HOIPs with potential applications for optoelectronics.

INTRODUCTION

Two-dimensional (2D) hybrid organic-inorganic perovskites (HOIPs) are gaining increasing attention owing to their remarkable optoelectronic/semiconducting properties and promise for application in transistors,[1,2] light-emitting diodes,[3-5] photovoltaics[6-10] and spintronics.[11,12] In contrast to $(CH_3NH_3)PbI_3$ (the archetypal 3D HOIP), the 2D analogs exhibit superior chemical stability and are structurally more diverse, with ample choices for the organic cation.[13,14] 2D HOIPs (general formula, A_2MX_4) can be viewed as self-assembled quantum well (QW) heterostructures,[15,16] where different semiconducting metal halide (MX_4^{2-}) perovskite and organic (A^+) cation layers allow for at least four distinct types of internal band alignments across the organic-inorganic interface.[17,18] These distinct band alignments offer multiple avenues to manipulate the overall optical/electronic functionalities,[17,19-21] to control carrier dynamics,[18] and to further tailor the relative energy levels and optoelectronic properties by compositional and dimensionality engineering of the inorganic layers[22] and/or tweaking the chemical nature of the organic cations.[23,24]

In the search for Pb-free 2D HOIPs, it is desirable to retain the electronic structure of Pb-based HOIPs, because their direct bandgap *p*-*p* transitions enabled by the Pb s^2 lone pair allow for strong optical absorption.[25] Isoelectronic cations to Pb^{II} such as Bi^{III} are naturally attractive candidates for exploring Pb-free HOIPs. However, <100>-oriented 2D HOIPs with layers of corner-sharing $M^{III}X_6$ (M= Bi^{III}; X=halogen) octahedra do not usually form because the M^{III} oxidation state necessitates energetically unfavorable metal vacancies for charge-balance between the organic cations and anionic metal halide layers. More commonly, Bi^{III} forms either discrete (monomeric/dimeric) or extended (polymeric) inorganic frameworks of corner-, edge-, or face-sharing MX_6 octahedra, resulting in a diverse family of halogenoanions (e.g., $[MX_4]^-$, $[MX_5]^{2-}$, $[MX_6]^{3-}$, $[M_2X_9]^{3-}$, $[M_2X_{11}]^{5-}$, $[M_3X_{11}]^{2-}$ $[M_3X_{12}]^{3-}$, $[M_4X_{18}]^{6-}$, $[M_5X_{18}]^{3-}$, $[M_6X_{22}]^{4-}$, and $[M_8X_{30}]^{6-}$) that are all characterized by a fully occupied M site.[26-29]

Another way of meeting the valence requirements is to incorporate two metals with distinct oxidation states. [30-36] To form double perovskites (DPs), both the metal sites additionally need to adopt stable octahedral coordination with a given halide ion. Various inorganic 3D DPs (e.g., $Cs_2M^IM^{III}X_6$; X=Cl, Br) containing a trivalent cation (M^{III}) such as Bi, Sb, In or Tl and a monovalent cation (M^I) such as Ag or Tl have been reported in the literature.[30-34] Most known 3D DPs of this family are characterized by large indirect bandgaps, while only a few possess direct bandgaps, e.g., $Cs_2AgInCl_6$[30] and Cs_2AgTlX_6 (X=Cl, Br)[34]. Although predicted to exhibit direct bandgaps, In(I)-based DPs such as

$Cs_2In^{I}M^{III}X_6$ (M^{III}=Bi/Sb; X=Cl, Br, I) are intrinsically unstable against oxidation into In(III)-based binary compounds.[37] Due to their expected lower band gaps, the iodide analogs are of special interest for semiconductors in optoelectronic applications. So far, however, this family of 3D DPs could not be extended to iodides with any of the above metal combinations;[36] Cs_2AgBiI_6 could only be kinetically stabilized in colloidal form by a post-synthetic anion exchange from the corresponding chlorides and bromides,[38] but the bulk counterpart has not been formed.

2D hybrid DPs may open a new avenue for stabilizing iodide-based DPs due to a number of possible choices of potentially stabilizing organic spacer cations. However, while a 2D DP bromide, $(BA)_4AgBiBr_8$ (BA = $CH_3(CH_2)_3NH_3^+$), with ordered Ag and Bi sites and electronically inactive BA^+ cations was recently reported,[39] the electronically desirable 2D mixed-metal iodide DPs have not yet been reported (to our knowledge, the only iodide DPs so far reported are based on mixed-valent homometal Au(I)/Au(III) iodides[40,41]). Strikingly, we find that their stabilization is not just a matter of changing the halide anion. In our own synthesis attempts of iodide-based Ag-Bi 2D DPs with BA^+ and related cations, competing 0D or 1D frameworks form instead (see below, as well as "Experimental methods" and Figure S4 in the supplementary information, SI). This is due to an intrinsic propensity of Bi to form low-dimensional non-perovskite hybrids, aggravated by the rareness of Ag in octahedral iodine coordination.

Here, we demonstrate the structure-directing influence of a specifically designed bi-functionalized organic spacer molecule—5,5'-diylbis(amino-ethyl)-[2,2'-bithiophene] (AE2T)—which, as a result of preferential edge-to-face aromatic interactions, acts as a template to stabilize the first example of a lead-free 2D mixed-metal DP iodide, i.e. $[AE2T]_2AgBiI_8$. Our work thus proves the value of employing specifically designed templating organic cation layers to stabilize unusual 2D perovskite phases that are often inaccessible using traditional spacer cations. Using spin-orbit coupled hybrid density functional theory (DFT), we also find that, in contrast to traditional spacer cations, in $[AE2T]_2AgBiI_8$, the frontier orbitals of AE2T are in close proximity to the inorganic band edges, resulting in a borderline type-I/II quantum well alignment, while the inorganic-derived bands are much less dispersive compared to related oligothiophene-Pb-based 2D HOIPs.[18] Experimentally, the optical transition in $[AE2T]_2AgBiI_8$ is weaker and broader compared to the sharp excitonic resonance commonly found in Pb-based HOIPs[42] and can be associated with a transition between equatorial I-*p* states in the valence band maximum (VBM) and hybridized equatorial I-*p* and Bi-*p*-orbitals in the conduction band minimum (CBM).

RESULTS AND DISCUSSION

Structural characteristics

Single crystals of $[AE2T]_2AgBiI_8$ were grown by slowly cooling a saturated aq. HI solution of stoichiometric amounts of AgI, BiI_3 and AE2T.2HI from 100 °C over 60 hours (see "Experimental methods" in SI for more details). AE2T.2HI was synthesized starting from thiophene-2-ethylamine (see scheme S1 and detailed description in SI).

$[AE2T]_2AgBiI_8$ crystallizes into a <100>-oriented perovskite, where each negatively charged inorganic perovskite layer is comprised of corner-sharing MI_6 [M=Ag or Bi] octahedra, with adjacent layers separated by layers of AE2T cations (Figure 1a). For $[AE2T]_2AgBiI_8$ crystals, two sets of reflections were observed from the CCD frames during the X-ray study at 298 K: one with well-defined, relatively sharp profile and the other with diffuse, streak-like character. The former corresponds to a monoclinic subcell (C2/c space group) with lattice parameters *a*=29.3654(14) Å, *b*=6.1473(3) Å, *c*=12.0494(6) Å and β=92.732(1)°, whereas the latter corresponds to a poorly resolved superstructure resulting in doubled *b*- and/or *a*-axes. The precession image of the reciprocal lattice reconstructed along the *hk*0 section (Figure S1) also reveals poorly resolved reflections forming streaks along *a** direction, plausibly due to a weak superstructure related to stacking of adjacent layers. [17,43,44] The adjacent MI_6 (M=Ag/Bi) octahedra in each inorganic layer are twisted with respect to each other, so that M-I-M bond angles substantially deviate from 180^0 [160.50(5)° and 159.43(5)°]. Within a given inorganic layer, any given square of four adjacent corner-sharing MI_6 octahedra (defined by four interconnected M-I-M bonds) is 'pulled-in' and 'pushed-out' along *b*- and *c*-axes, respectively, or vice versa. The distortion pattern of each square fixes the nearest-neighboring square of octahedra to be in the opposite pattern (Figure 1b). The distortions in each inorganic layer (*b*-*c* plane) are, therefore, fully ordered; however, the adjacent layers are not in registry with each other. Such diffuse scattering arising from a poorly ordered superstructure is not uncommon among layered 2D HOIPs, having also been observed earlier in (3-fluorophenethylammonium)$_2SnI_4$,[43] (2-fluorophenethylammonium)$_2SnI_4$,[43] (AE4T)$PbBr_4$,[17] and $[AE4T]Bi_{2/3}\square_{1/3}I_4$,[44] whose structures have been refined using a similar subcell approach. The $[AE2T]_2AgBiI_8$ crystal structure can be solved adequately using the C2/c subcell (see Table S1 in SI), but no meaningful structure solution could be obtained using the larger supercell approach, likely due to the poorly resolved X-ray peaks (and ordering) corresponding to the larger cell.

Within the inorganic layer of $[AE2T]_2AgBiI_8$, Ag and Bi cations do not appear to exhibit long-range order on the M site and are instead successfully modeled as being statistically distributed, where the chemical occupancy of Ag and Bi refines to ~ 0.5 for each. Consistently, both EDS and XPS quantitative analysis on single crystals confirm nearly equal proportions of Ag and Bi (Figures S2 and S3, SI). We note that the apparent absence of long-range order in diffraction does not rule out the existence of local order (or order within a given layer, as opposed to registry between the layers), as indicated by our DFT results below. Each equatorial iodine in the inorganic layer is disordered over two symmetry-related sites with an occupancy of 0.5. The disorder of equatorial iodine atoms is a consequence of the poorly resolved superstructure associated with the lack of registry between adjacent inorganic layers. In the subcell model, the two unique patterns of square distortion are superimposed with equal probability, resulting in an apparent disorder of equatorial iodine atoms (Figure 1b). The lack of registry between adjacent inorganic layers is plausible given that the ethylammonium tethering groups of the AE2T cations, nominally interacting with the distorted square of MI_6 octahedra

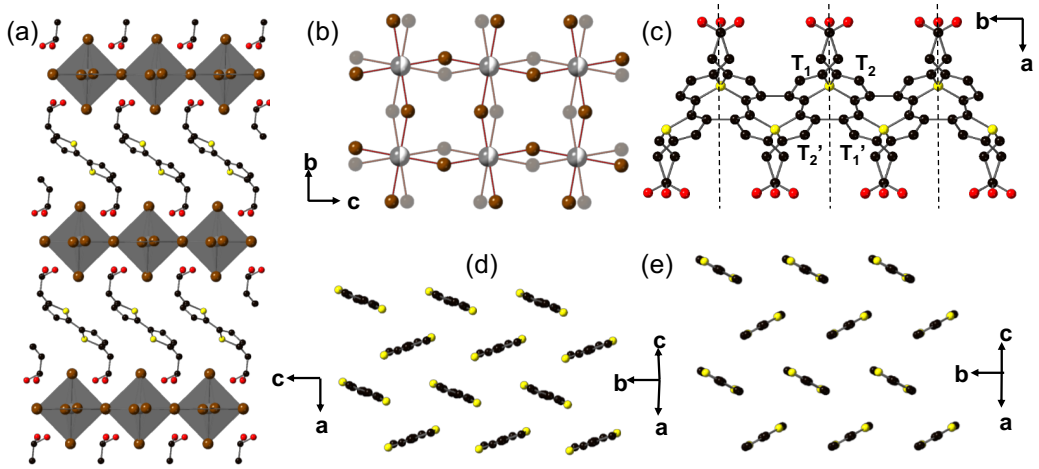

Figure 1. a) Schematic showing the 2D layered crystal structure (C2/c space group) of the $[AE2T]_2AgBiI_8$ DP. b) Two distorted frameworks of interconnected equatorial M-I_{eq}-M bonds superimpose to give rise to two sets of half-occupied equatorial iodine atoms (denoted by solid and shaded brown spheres). Randomly occupied Ag/Bi sites are shown as two-colored spheres. c) View of AE2T cations disordered across the c-glide plane (indicated as dotted lines) extending as polymeric ribbons along the b-axis. Considering only one set of disordered bithiophene moieties, the herringbone packing arrangement in a single organic layer of d) $[AE2T]_2AgBiI_8$ closely matches that in e) 'neat' 2,2'-bithiophene crystals along a similar viewing direction. Ethyl ammonium groups are omitted in (d) for clarity. Black, red and yellow spheres denote C, N and S atoms, respectively.

through hydrogen bonding with nearest iodine atoms, are flexible enough to adopt different conformations corresponding to the two different square distortions.

In the organic layer, all the carbon atoms (except the terminal one closest to the nitrogen) and nitrogen atoms of the AE2T cation are disordered across the c-glide plane (Figure 1c). The asymmetric unit contains two unique thiophene rings (T_1 and T_2), and the other half of each bithiophene moiety (i.e., T_1' and T_2') is generated by 2_1 symmetry. The two thiophene rings within each AE2T moiety are nearly coplanar with a dihedral angle of 0.66° between least-squares best planes containing the individual thiophene rings. The adjacent thiophene rings adopt an 'anti' configuration (see Figure 1c), as typically found in neat organic crystals of unsubstituted bithiophene molecules[45] as well as related hybrids incorporating substituted bithiophene cations.[46] The disorder for the AE2T cation is also consistent with the poorly defined/resolved superstructure—i.e., the diffuse scattering along a^* doubles the b-axis, but in the subcell ($\sim 1_b \times 2_c$) model considered here, the two half-occupied (i.e., equal probability) configurations of the AE2T backbone become superimposed to extend as ribbons along the b-direction (Figure 1c). Similar disordering of the organic cation across symmetry elements was found in $[AE4T]Bi_{2/3}\square_{1/3}I_4$, which also exhibits a poorly resolved superstructure.[44]

X-ray data collected at 100 K for $[AE2T]_2AgBiI_8$ also exhibits a diffuse scattering due to poorly resolved superstructure. The 2D perovskite structure at 100 K can be solved adequately in a monoclinic C2/c subcell with lattice parameters a=28.951(3) Å, b=6.0992(6) Å, c=11.9821(12) Å and β=92.266(2) ° (see Table S1 in SI), and features disordered inorganic and organic layers similar to the 298 K structure.

Templating influence of oligothiophene spacer cations

In 2000, Mitzi reported the unique templating influence of an oligothiophene-based diammonium cation in stabilizing an unusual Bi-deficient <100>-oriented 2D HOIP, $[AE4T]Bi_{2/3}\square_{1/3}I_4$ (AE4T: 5,5‴-bis-(aminoethyl)-2,2′:5′,2″:5″,2‴-quaterthiophene).[44] The latter HOIP features 2D layers of corner-sharing distorted BiI_6 octahedra with randomly distributed Bi-vacancies and represents the first member of a new family of metal-deficient 2D HOIPs with $[M^{n+}_{2/n}\square_{(n-2)/n}X_4]^{2-}$ layers (□=M-site vacancy). The templating role of the AE4T cation was ascribed to edge-to-face (tilted-T type) intermolecular aromatic interactions that are strong enough to compensate for an otherwise unfavorable formation enthalpy of a substantial density of Bi-vacancies (i.e., 1/3 of the sites) within the perovskite layer. Notably, another complex but relatively flexible diammonium organic cation, [1,6-bis[5′-(2″-aminoethyl)-2′-thienyl]hexane], wherein the two terminal thienyl rings are separated by a hexyl chain (as opposed to a bithiophene unit in AE4T), leads to a one dimensional (1D) hybrid with corner-sharing zigzag chains of distorted BiI_6 octahedra,[47] emphasizing the importance of structural rigidity in addition to the aromatic interactions for stabilizing these more complex metal-deficient 2D perovskites.

As the number of thiophene rings within the oligothiophene moiety is systematically decreased from four (AE4T) to three (AE3T) and down to two (AE2T), the strength of aromatic interactions is expected to decrease, thereby influencing the overall templating ability. For instance, free-energy calculations show a decreasing gas-phase interaction enthalpy going from anthracene to naphthalene to benzene dimers, accompanied by a change in preference for π-stacked structure in anthracene dimers to tilted-T type structure in benzene dimers.[48] In the current study, we focus on the 2D DP with 1:1 mixture of Bi and Ag atoms, to achieve an average +2 oxidation state for the metal site without vacancies. Such structures are still subject to instability due to the availability of more stable alternative phases (i.e., those with 0D or 1D Bi-I frameworks). To stabilize the 2D structure, we have employed the smaller (relative to AE4T) but still rigid AE2T cation and find that the ar-

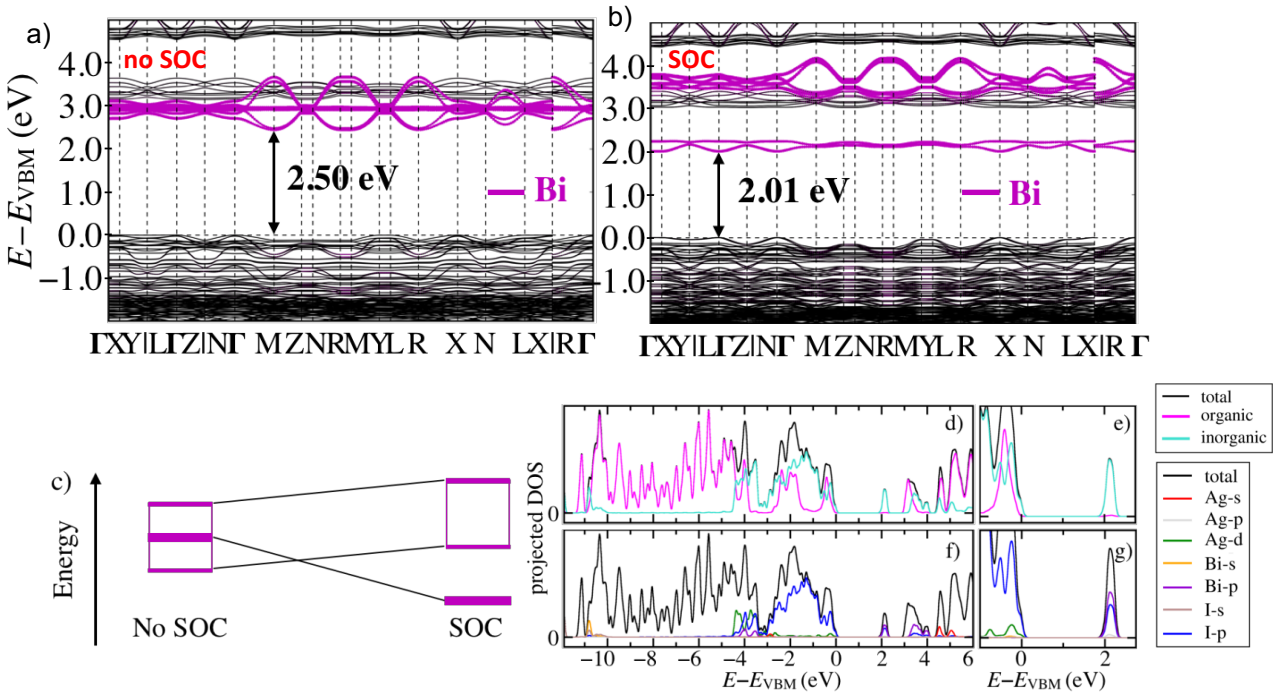

Figure 2: DFT-HSE06 band structure of $[AE2T]_2AgBiI_8$ a) without and b) with spin-orbit coupling (SOC). The contributions of the Bi-6*p*-orbitals are identified (purple) and the zero in energy is set to the VBM. c) Schematic molecular orbital diagram for the splitting of the Bi-6*p* orbitals into $p_{1/2}$ and $p_{3/2}$ contributions under SOC. d) DFT-HSE06+SOC total density of states (DOS, black), and partial DOS projected onto the atoms of the organic compound (magenta) and the inorganic compound (turquoise). e) Magnified region around band edges from (d). f) Total DOS (black) and Ag-s (red), Ag-p (grey), Ag-d (green), Bi-s (orange), Bi-p (purple), I-s (brown) and I-p (blue) partial DOS. g) Magnified region around band edges from (f).

omatic interactions in AE2T are sufficiently strong to template the targeted lead-free 2D DP iodide, i.e. $[AE2T]_2AgBiI_8$. AE2T cations were selected here (as opposed to AE4T) because they are more readily employed (i.e., exhibit higher solubility) for synthesizing the hybrid 2D DP.

The bithiophene moieties within a single organic layer of $[AE2T]_2AgBiI_8$ are arranged in a herringbone pattern (Figure 1d) with edge-to-face (tilted-T type) aromatic interactions, similar to that observed in $[AE4T]Bi_{2/3}\square_{1/3}I_4$ and in the 'neat' 2,2'-bithiophene organic crystals (Figure 1e).[45] The herringbone angle between the least-squares best planes through the adjacent AE2T cations (excluding the terminal ethylammonium tethering units) in $[AE2T]_2AgBiI_8$ is 42.97°, which can be compared to the 58.35° value in bithiophene crystals. Despite being in a very different chemical environment (i.e., in between metal halide layers), the preferred herringbone arrangement of bithiophene units within 2D layers, favored by the edge-to-face interactions, is able to template the formation of 2D metal halide layers in $[AE2T]_2AgBiI_8$. In a gas-phase

benzene dimer, the stable aromatic interaction is also of the tilted-T type, with interaction energy of about -2 kcal/mol[48], which is comparable to a weak hydrogen bond. A similar order of magnitude for the interaction energy can be expected for the tilted-T type interactions of neighboring AE2T cations in $[AE2T]_2AgBiI_8$.

Notably, we found that a linear *n*-butylammonium (BA) cation, as used in $(BA)_4AgBiBr_8$ DP,[39] or its diammonium analog, butane-1,4-diammonium (BDA), could not stabilize a 2D DP iodide under synthesis conditions similar to those used to form $[AE2T]_2AgBiI_8$. Instead, a hybrid Bi iodide with more typical 0D (or 1D) connectivity crystallizes from the solution containing stoichiometric amounts of AgI, BiI_3, and BA (or BDA) (see Experimental methods and Figure S4 in SI for more details). Moreover, an asymmetrical, mono-substituted bithiophene cation with a sulfur ethylammonium tethering group (AESBT: $(C_4S)_2S(CH_2)_2NH^{3+}$) was previously shown to form non-perovskite hybrids with Pb and Bi, namely, $(AESBT)_4Pb_3I_{10}$ and $(AESBT)_3Bi_2I_9$.[46] $(AESBT)_4Pb_3I_{10}$ exhibits a herringbone molecular packing of organic cations while $(AESBT)_3Bi_2I_9$ exhibits a mixed packing with alternating herringbone and k-type arrangements.[46] Therefore, in addition to the associated aromatic interactions and the hydrogen bonding interactions of ammonium tethering groups, mono- vs. bi-substitution of the spacer cation impacts the stability of the 2D perovskite structure. These observations emphasize that multiple aspects of the AE2T cation synergistically converge to template an otherwise unstable 2D DP iodide—i.e., strong intermolecular edge-to-face aromatic interactions that intrinsically drive AE2T cations to pack into 2D herringbone layers, structural rigidity of the AE2T backbone, and tethering ammonium groups on either end of the bithiophene moiety that drive self-assembly of 2D DP layers via hydrogen bonding interactions with the latter.

It is further noted that both the metal sites in a DP halide must adopt stable octahedral coordination with the halide. Bi typically exhibits octahedral coordination with I, whereas Ag by itself rarely exhibits octahedral iodine coordination, but rather usually prefers tetrahedral coordination. In contrast, six-coordinated Ag is found often in bromides, the simplest example being AgBr with a rock-

salt structure. However, Bi can occasionally facilitate octahedral coordination of Ag with I as found in $AgBiI_4$ and Ag_3BiI_6, where Ag and Bi exhibit site-disorder.[49] This site mixing, in conjunction with the templating influence from AE2T, helps to stabilize the unprecedented iodide-based 2D DP structure found for $[AE2T]_2AgBiI_8$.

First-principles calculations.

To understand the electronic structure of the Ag-Bi 2D perovskite framework, we carried out first principles DFT calculations within the all-electron electronic structure code FHI-aims.[50-54] We first optimized geometries for $[AE2T]_2AgBiI_8$ until all residual forces on the nuclei were below 0.005 eV/Å in magnitude, based on the experimental structure and using the PBE exchange-correlation functional[55] plus the Tkatchenko-Scheffler (TS) pairwise dispersion scheme,[56] "tight" basis sets and other numerical defaults within FHI-aims. The electronic structure of the perovskite is then investigated based on the DFT-PBE+TS relaxed geometries using the established HSE06 hybrid density functional with fixed values α=0.25 and ω=0.11 $bohr^{-1}$ for the exchange mixing parameter and range separation parameter, respectively.[57-59] The accuracy of this set of approaches for oligothiophene based 2D perovskites was demonstrated by extensive validation in Ref. 18 and its SI. Spin-orbit coupling (SOC) is treated using a second-variational, non-self-consistent approach, rendering the expensive but necessary hybrid DFT band structure calculations computationally feasible.[60] In Ref. 60, a broad analysis of different computational approaches to SOC shows that the non-self-consistent approach remains qualitatively accurate even for Bi, but quantitative differences to a self-consistent SOC treatment become significant (about 10% of the overall SOC splitting for the Bi-6*p* derived states). In Figures S5 and S6 (SI), we therefore assess the accuracy of the SOC treatment for Bi-6*p* derived conduction band states specifically for a simpler Ag-Bi based DP, $Cs_2AgBiCl_6$,[61] comparing to a fully self-consistent implementation including $p_{1/2}$ local orbitals in the basis set, as implemented in the all-electron augmented plane wave code WIEN2K.[62] This analysis reveals a relative accuracy of the Bi 6-*p* derived states of about 0.4 eV, similar to the expected quality of the HSE06 density functional[63-65] and supporting our overall approach.

In order to accurately model the octahedral distortion pattern in the inorganic layers (Fig. 1b), a (2 × 2) supercell is required (as in the case of oligothiophene-containing Pb-based perovskites[18]). Within the supercell, we chose a checkerboard-like Ag-Bi pattern (see Figures S7a and c). We note that different Ag-Bi patterns are possible in principle. The experimental XRD pattern does not clarify this point since the site disorder assumed in the refinement can result as a consequence of lack of registry between different Ag-Bi planes. Within the (2 × 2) supercell, only one other Ag-Bi arrangement is possible, consisting of adjacent rows of Ag- and Bi-containing iodide octahedra (Figures S7b and d). As shown in the SI, our calculations indicate significantly greater structural and energetic stability for the checkerboard-like pattern, i.e., a significant tendency of Ag and Bi to form a locally well-ordered arrangement. This is consistent with several literature reports for 3D DPs, [66-68]all of which indicate high ordering energies. In Ref. 68 a first-principles cluster expansion of the 3D compound $Cs_2AgBiBr_6$ shows that the onset of meaningful Ag-Bi disorder occurs only above ~1000 K, significantly higher than the expected overall stability range of the 2D DP investigated here. Both our own results and the literature therefore point towards the checkerboard-like Ag-Bi arrangement within a single plane as the dominant structural motif to be considered. After structure relaxation, the predicted *b* and *c* lattice parameters of this model agree with the experimental lattice parameters (at 100 K) to within 0.4% for the *b* and *c* lattice parameters, and to within 2.7% for the *a* lattice parameter (see Table S3). Each metal atom has one long and one short axial bond. Long and short Bi-I_{ax} bond lengths in the supercell average to 3.29 Å and 3.05 Å, respectively, whereas long and short Ag-I_{ax} bond lengths average to 3.20 Å and 2.89 Å, respectively. Furthermore, the orientation of the short vs. long axial bonds (upwards or downwards relative to the inorganic plane) alternates among sites within the inorganic layer. The Bi-I bond lengths found here are typical of those encountered in bismuth iodide hybrids.[44,46] In contrast, Ag rarely exhibits octahedral coordination with I, a few examples being Tl_2AgI_3 (Ag-I: 3.126 Å) with a regular coordination [69] and $Ag_4I_2SeO_4$ (Ag-I: 2.878 Å - 3.458 Å) with a distorted coordination with O and I.[70] These Ag-I bond lengths are comparable to those found in our relaxed structure.

In the experimental subcell model considered here, axial M-I bonds refine to an average value of 3.0705(8) Å, due to the assumed random distribution of Ag and Bi. The axial I in the 298 K structure can, however, be successfully split during structural refinement into four distinguishable sites with a fixed chemical occupancy of 0.25 for each, which may be assigned to the axial bond types, Bi-I_{ax} (3.334 (17) Å and 3.075(17) Å) and Ag-I_{ax} (3.080(17) Å and 2.848(5)) (Figure S8), in good qualitative agreement with the computationally-derived values. Other predicted structural details are also in close agreement with the experimental structure (see Figures S8 and S9 for details). Comparing to the $(BA)_4AgBiBr_8$ DP,[39] very short axial Ag-Br bonds were found, but asymmetric bond lengths for Bi-Br_{ax} and Ag-Br_{ax} were only found for its high-dimensional analogue with mixed BA and Cs cations.

Figure 2a and 2b show the HSE06 band structure of $[AE2T]_2AgBiI_8$. Without the inclusion of spin-orbit coupling (SOC, Figure 2a), the predicted bandgap is indirect (2.5 eV). The necessity to include SOC for a correct description of Pb- and Bi-based HOIPs is well established.[18,71-73] Accordingly, and in qualitative agreement with observations for $Cs_2AgBiBr_6$ and $Cs_2AgBiCl_6$, [61,71] inclusion of SOC (Figure 2b and c) leads to a separation within the Bi-6*p* derived conduction band, resulting in a split-off conduction band. Consistent with analogous assignments for 3D DPs,[71] we attribute the split-off conduction band, which shifts down, to Bi-$6p_{1/2}$ derived states. The more disperse bands, which shift upwards, are attributed to Bi-$6p_{3/2}$ derived states. As a result of the shift, the conduction band minimum with SOC is found at the Γ point and the bandgap including SOC (2.01 eV) is direct, in contrast to the case without SOC. Both the CBM and the VBM are isoenergetic to within 10 meV between X (π/a, 0, 0) and Γ (0,0,0). The presence of the CBM

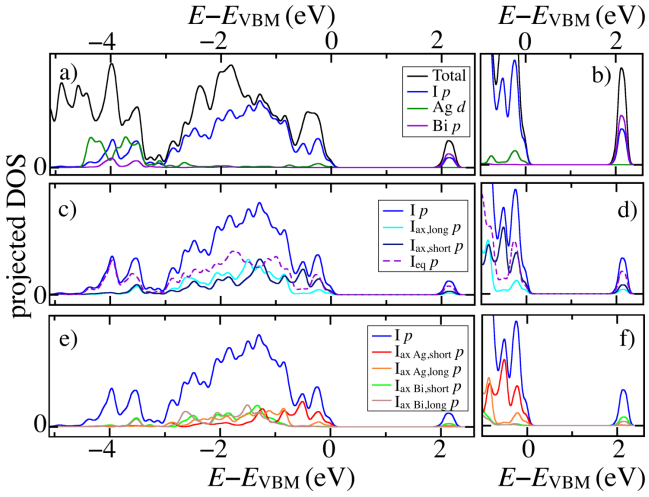

Figure 4: The DFT-HSE06+SOC DOS for $[AE2T]_2AgBiI_8$. a) Decomposition of the total DOS (black) into I-p (blue), Ag-d (green) and Bi-p (purple) orbital contributions (an enlarged version is shown in Figure 2c). b) Magnification of band edges from (a). c) Further separation of the I-p contribution according to I atoms bonded axially to the metal atoms with short ($I_{ax,short}$, dark blue) and long bonds ($I_{ax,long}$, light blue), as well as equatorial I-atoms (I_{eq}, dashed purple) that connect Ag and Bi within the inorganic sheets. d) Magnification of the band edges from (c). e) I-p contribution to DOS from axially bound I, projected onto Ag-bound axial I with short ($I_{ax,\,Ag,\,short}$, red) and long ($I_{ax\ Ag,\ long}$, orange) bonds and onto Bi-bound axial I with short ($I_{ax\ Bi,\ short}$, green) and long ($I_{ax\ Bi,\ long}$, brown) bonds. f) Magnification of the band edges from (e).

and VBM at Γ is likely the result of band back folding, as seen in the example of a model (2 × 1) unit cell in the SI (Figure S10). Connor *et al.*[39] showed that the direct bandgap in 2D $(BA)_4AgBiBr_8$ DP, compared to the indirect one found in higher-dimensional (i.e., n=2 and n=∞) AgBi-based bromide DPs, is the result of dimensionality reduction.[39] Replacing Pb by Ag-Bi in $Cs_2Pb_2Br_6$ has been observed to lead to less dispersive bands in the conduction band of the Ag-Bi-compound due to confinement of the frontier orbitals to either Ag (VBM) or Bi (CBM), with only 2nd-nearest neighbor cation interactions compared to nearest-neighbor interactions in Pb-based compounds[67]. In agreement with this observation, the bands in the conduction band of $[AE2T]_2AgBiI_8$ are relatively non-dispersive (i.e., "flat") compared to the band structures of the direct-bandgap oligothiophene-containing Pb-based HOIPs[18]—i.e., flat enough that the conduction band becomes isolated.

To understand the character of the frontier orbitals, we further investigated the DOS projected onto the organic and inorganic frameworks of $[AE2T]_2AgBiI_8$ (Figures 2b and c). The VBM and CBM are formed by the inorganic layers, but with the organic HOMO almost degenerate with, i.e., ~0.03 eV below, the inorganic VBM in $[AE2T]_2AgBiI_8$. Nominally, this alignment represents a type Ib heterojunction (in the notation of Ref. 18); however, given the remaining accuracy limits of hybrid DFT calculations, it cannot be distinguished from a type IIb heterojunction. Apart from the flatter inorganic-derived bands, the electronic structure of $[AE2T]_2AgBiI_8$ is hence similar to the electronic structure exhibited by or expected from the oligothiophene-Pb-based HOIPs.[18] Figures 2d and e show contributions to the inorganic frontier orbitals of $[AE2T]_2AgBiI_8$ resolved according to element and orbital character. The VBM is dominated by I-*p* states, with contributions of Ag-*d* states. The CBM is predominantly comprised of Bi-*p* and I-*p* (analogous to the Pb-*p* and I-*p* makeup for the Pb system).[74] The composition of the frontier levels in $[AE2T]_2AgBiI_8$ is also qualitatively similar to that of the $(BA)_4AgBiBr_8$ DP.

Structural and optical characterization

Figure 3a shows the PXRD patterns of polycrystalline powders and thin films of $[AE2T]_2AgBiI_8$ (prepared as described in the SI) compared to a reference pattern simulated from the experimental room-temperature single crystal structure. The PXRD patterns agree well with the simulated pattern with no detectable impurities to within the instrumental limit. The absorption spectra of the $[AE2T]_2AgBiI_8$ film at 293 K and 78 K (Figure 3b) are nearly superimposable, with a slight reduction in the absorbance at energies greater than 3.6 eV. The lowest-energy absorption peak is a broad feature centered around 2.3 eV, in contrast to the sharp excitonic peak observed for the analogous Pb-based HOIP.[17,42] From the corresponding Tauc plot (at 293 K), shown in Figure 3b, we find a direct bandgap of 2.00(2) eV for $[AE2T]_2AgBiI_8$. The exceptional agreement with the theoretical bandgap of 2.01 eV is likely fortuitous in view of the remaining uncertainty from both the computational SOC treatment and the HSE06 density functional, as described above. A direct bandgap was also

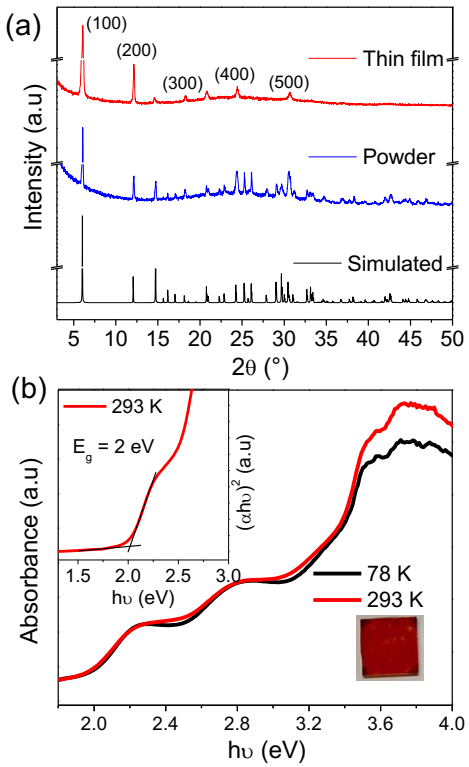

Figure 3. a) PXRD patterns of thin films and powdered crystals of $[AE2T]_2AgBiI_8$, along with a simulated pattern (derived from the single crystal structure) for comparison. b) Absorption spectra for thin films of $[AE2T]_2AgBiI_8$ recorded at 78 K and 293 K. The upper and lower insets show the corresponding Tauc plot at 293 K and photograph of the thin film, respectively.

observed for the 2D $(BA)_4AgBiBr_8$ DP, but with a higher value (2.85 eV)[39] that, as mentioned above, can mostly be attributed to the lighter halide anion. Similar to our findings, the lowest energy absorption feature appears broad for $(BA)_4AgBiBr_8$, as compared to the narrow excitonic peaks observed in 2D lead halide perovskites. While it would be tempting to interpret the lowest-energy absorption peak in $[AE2T]_2AgBiI_8$ as a broadened excitonic feature, this interpretation is not supported by its very weak temperature dependence (Figure 3b), as well as by the absence of corresponding PL (see below); also in line with the interpretation of the equivalent peak for $(BA)_4AgBiBr_8$.[39]

Interestingly, the computed absorption spectra for $[AE2T]_2AgBiI_8$ in Figure S11 are remarkably similar to the experimentally determined curves. The spectra in Figure S11 are calculated at the DFT-HSE06+SOC level of theory and employing the independent-particle approximation, using the same implementation as in Ref. 65 and neglecting any excitonic effects. Following this approximation, the first absorption peak would be related to the *inorganic* components at the onsets of the VBM and CBM, since there is no discernible partial contribution of the organic moiety to the first DOS peak that defines the CBM in Figures 2b and c. The inorganic DOS contributions are further decomposed in Figures 4a-f, revealing the inorganic VBM to be derived from Ag-*d* and I-*p* orbitals, whereas the CBM originates from Bi-*p* and I-*p* (Figures 4a and b). A similar decomposition for a Br-based DP was performed in Ref. 39, where the analogous near-band-edge absorption was associated with "considerable Ag to Bi charge-transfer (CT) character". In line with an analysis of Au(I)-Au(III) DP,[41] the actual absorption in $[AE2T]_2AgBiI_8$ is expected to be mediated by the halide ion connecting Ag and Bi. The partial DOS in Figures 4a and b shows that a direct metal-to-metal CT cannot be responsible for the spectra computed in Figure S11—i.e., the Ag-*d* component (VBM) is zero in the CBM, and *vice versa* for Bi-*p* in the CBM, leaving little room for a non-zero metal-to-metal transition dipole matrix element.

A closer analysis of the I-*p* DOS (Figures 4c-d) reveals considerable contributions of the equatorially bonded I atoms (I_{eq}), which connect Ag and Bi atoms, to both the VBM and CBM. The observed absorption near the band edges is therefore consistent with transitions between I_{eq}-*p* states in the VBM and hybridized I_{eq}-*p* and Bi-*p* states in the conduction band. Finally, the axially bonded I atoms, I_{ax}, cannot contribute to near-band-edge absorption; their PDOS (Figures 4e-f) shows that I_{ax} atoms bonded to Ag contribute to the VBM, but not the CBM, and *vice versa* for I_{ax} atoms bonded to Bi. This is somewhat in contrast to the conventional picture in Pb-based HOIPs where the VBM derives from an antibonding combination of Pb 6*s* and I 5*p* states, while the CBM mainly exhibits contributions from Pb 6*p* and small contributions from equatorial I *s* and axial I *p* states.[74] This band structure is thought to allow for a CT-like direct *p*-*p*-transition *within the same metal* (i.e. Pb).[25,39,75]

Despite its predicted direct bandgap, we find that $[AE2T]_2AgBiI_8$ is barely luminescent at room temperature and even at 78 K. In contrast, Pb-based HOIPs exhibit a strong and sharp excitonic emission near room temperature.[17,42] Given the band structure and partial DOS in Figure 2, one possible explanation for quenching could be type IIb band alignment[18], i.e., separate VBM (organic) and CBM (inorganic), a scenario which is well within the accuracy limits of current theory. However, the lack of PL is also consistent with the case for $(BA)_4AgBiBr_8$,[39] wherein type II alignment seems much less likely and yet PL is completely quenched near room temperature (a broad and weak defect-mediated emission appears only below 80 K). A tentative explanation for the absence of PL is suggested by the character of VBM (I_{eq} and Ag derived) and CBM (I_{eq} and Bi derived) in Figure 4, indicating that the photogenerated holes would be primarily located on Ag-containing octahedra, whereas the electrons would be located primarily on Bi-containing octahedra. In this scenario, the optical excitations would survive for a long time due to lack of radiative recombination. Indeed, our transient absorption spectroscopy (TAS) measurements on $[AE2T]_2AgBiI_8$ thin films reveal a decay of photobleaching through a multistep relaxation process (Figure S12). Within the first few picoseconds, the transient bleaching signal decays but does not completely vanish. After a fast relaxation in the first few picoseconds, the bleaching signal survives longer than 6 ns (beyond the experimental time window), suggesting the initial transfer of excitations into long-lived dark states.

CONCLUSIONS

In conclusion, we demonstrate that aromatic interactions in specifically designed bifunctional AE2T spacer cations can template unprecedented 2D DP layers of Ag-Bi iodide, otherwise inaccessible with more traditional (i.e., less rigid and lacking substantial aromatic-aromatic interaction) spacer cations. Transition from bromide to iodide leads to a reduction in band gap to 2.00(2) eV, the smallest value reported to date for 2D DPs. However, in agreement with a previous observation for the 2D Ag-Bi DP bromide,[39] we show that replacing Pb by Ag-Bi leads to flatter electronic bands, a lack of exciton features and strongly quenched PL (at least for temperatures >80 K). We determine that the broad, lowest-energy direct transition in $[AE2T]_2AgBiI_8$ occurs between nominally inorganic-derived states at band extrema, and propose that the lack of considerable band-edge PL likely derives from spatial localization/separation of photoexcited holes and electrons in the vicinity of Ag and Bi, respectively. $[AE2T]_2AgBiI_8$ also differs from most other related 2D HOIPs with traditional spacer cations by the proximity of organic AE2T frontier orbitals to the inorganic VBM and CBM and the formation of a borderline type Ib/type IIb internal quantum well structure. Our present work emphasizes that specifically designed organic cations can perform a double role within 2D perovskites: stabilizing desirable but otherwise unobtainable inorganic frameworks and simultaneously tuning the nature of frontier orbitals to afford specific optoelectronic character. This latter point has been explored recently for the Pb-based systems,[18] and will be pursued for the Ag/Bi analogs in future work.

ASSOCIATED CONTENT

Supporting Information. Synthesis details of AE2T.2HI salt; experimental and computational methods; 298 K and 100 K single crystal structural data for $[AE2T]_2AgBiI_8$; XPS and FESEM characterization of $[AE2T]_2AgBiI_8$ single crystals; de-

tails of $[AE2T]_2AgBiI_8$ theoretical structure; comparison of experimental and theoretical lattice constants, bond lengths and bond angles; calculated absorption coefficient; and transient absorption spectra along with corresponding decay kinetics for $[AE2T]_2AgBiI_8$ thin film.
$[AE2T]_2AgBiI_8$_100 K (CIF)
$[AE2T]_2AgBiI_8$_298 K (CIF)

AUTHOR INFORMATION

Corresponding Author

* email: david.mitzi@duke.edu

Notes

Authors declare no competing financial interest.

ACKNOWLEDGMENT

M.K.J., D.B.M., S.M.J., V.B., C. L., D.D., W.Y., S.D., and K.G. acknowledge support from the NSF DMREF program (HybriD^3) under grant numbers DMR-1729297, DMR-1728921 and DMR-1729383. An award of computer time was provided by the INCITE program. This research used resources of the Argonne Leadership Computing Facility, which is a DOE Office of Science User Facility supported under Contract DE-AC02-06CH11357. SMJ thanks the Deutsche Forschungsgemeinschaft (DFG, German Research Foundation) for a postdoctoral fellowship, grant number 393196393.

REFERENCES

(1) Mitzi, D. B.; Dimitrakopoulos, C. D.; Rosner, J.; Medeiros, D. R.; Xu, Z.; Noyan, C. Hybrid Field-Effect Transistor Based on a Low-Temperature Melt-Processed Channel Layer. *Adv. Mater.* **2002**, *14*, 1772.

(2) Kagan, C. R.; Mitzi, D. B.; Dimitrakopoulos, C. D. Organic-Inorganic Hybrid Materials as Semiconducting Channels in Thin-Film Field-Effect Transistors. *Science* **1999**, *286*, 945.

(3) Van Le, Q.; Jang, H. W.; Kim, S. Y. Recent Advances toward High-Efficiency Halide Perovskite Light-Emitting Diodes: Review and Perspective. *Small Methods* **2018**, *2*, 1700419.

(4) Zhao, B.; Bai, S.; Kim, V.; Lamboll, R.; Shivanna, R.; Auras, F.; Richter, J. M.; Yang, L.; Dai, L.; Alsari, M.; She, X.-J.; Liang, L.; Zhang, J.; Lilliu, S.; Gao, P.; Snaith, H. J.; Wang, J.; Greenham, N. C.; Friend, R. H.; Di, D. High-efficiency perovskite–polymer bulk heterostructure light-emitting diodes. *Nat. Photonics* **2018**, *12*, 783.

(5) Zhao, X.; Ng, J. D. A.; Friend, R. H.; Tan, Z.-K. Opportunities and Challenges in Perovskite Light-Emitting Devices. *ACS Photonics* **2018**, *5*, 3866.

(6) Tsai, H.; Nie, W.; Blancon, J.-C.; Stoumpos, C. C.; Asadpour, R.; Harutyunyan, B.; Neukirch, A. J.; Verduzco, R.; Crochet, J. J.; Tretiak, S.; Pedesseau, L.; Even, J.; Alam, M. A.; Gupta, G.; Lou, J.; Ajayan, P. M.; Bedzyk, M. J.; Kanatzidis, M. G.; Mohite, A. D. High-efficiency two-dimensional Ruddlesden–Popper perovskite solar cells. *Nature* **2016**, *536*, 312.

(7) Smith, I. C.; Hoke, E. T.; Solis-Ibarra, D.; McGehee, M. D.; Karunadasa, H. I. A Layered Hybrid Perovskite Solar-Cell Absorber with Enhanced Moisture Stability. *Angew. Chem.* **2014**, *126*, 11414.

(8) Cao, D. H.; Stoumpos, C. C.; Farha, O. K.; Hupp, J. T.; Kanatzidis, M. G. 2D Homologous Perovskites as Light-Absorbing Materials for Solar Cell Applications. *J. Amer. Chem. Soc.* **2015**, *137*, 7843.

(9) Mao, L.; Ke, W.; Pedesseau, L.; Wu, Y.; Katan, C.; Even, J.; Wasielewski, M. R.; Stoumpos, C. C.; Kanatzidis, M. G. Hybrid Dion–Jacobson 2D Lead Iodide Perovskites. *J. Amer. Chem. Soc.* **2018**, *140*, 3775.

(10) Li, Y.; Milić, J. V.; Ummadisingu, A.; Seo, J.-Y.; Im, J.-H.; Kim, H.-S.; Liu, Y.; Dar, M. I.; Zakeeruddin, S. M.; Wang, P.; Hagfeldt, A.; Grätzel, M. Bifunctional Organic Spacers for Formamidinium-Based Hybrid Dion–Jacobson Two-Dimensional Perovskite Solar Cells. *Nano Lett.* **2019**, *19*, 150.

(11) Yin, J.; Maity, P.; Xu, L.; El-Zohry, A. M.; Li, H.; Bakr, O. M.; Brédas, J.-L.; Mohammed, O. F. Layer-Dependent Rashba Band Splitting in 2D Hybrid Perovskites. *Chem. Mater.* **2018**, *30*, 8538.

(12) Zhai, Y.; Baniya, S.; Zhang, C.; Li, J.; Haney, P.; Sheng, C.-X.; Ehrenfreund, E.; Vardeny, Z. V. Giant Rashba splitting in 2D organic-inorganic halide perovskites measured by transient spectroscopies. *Science Adv.* **2017**, *3*, e1700704.

(13) Saparov, B.; Mitzi, D. B. Organic–Inorganic Perovskites: Structural Versatility for Functional Materials Design. *Chem. Rev.* **2016**, *116*, 4558.

(14) Mao, L.; Stoumpos, C. C.; Kanatzidis, M. G. Two-Dimensional Hybrid Halide Perovskites: Principles and Promises. *J. Amer. Chem. Soc.* **2018**, *141*, 1171.

(15) Mitzi, D. B.; Chondroudis, K.; Kagan, C. R. Organic-inorganic electronics. *IBM J. Res. Dev.* **2001**, *45*, 29.

(16) Hong, X.; Ishihara, T.; Nurmikko, A. V. Photoconductivity and electroluminescence in lead iodide based natural quantum well structures. *Solid State Commun.* **1992**, *84*, 657.

(17) Mitzi, D. B.; Chondroudis, K.; Kagan, C. R. Design, Structure, and Optical Properties of Organic–Inorganic Perovskites Containing an Oligothiophene Chromophore. *Inorg. Chem.* **1999**, *38*, 6246.

(18) Liu, C.; Huhn, W.; Du, K.-Z.; Vazquez-Mayagoitia, A.; Dirkes, D.; You, W.; Kanai, Y.; Mitzi, D. B.; Blum, V. Tunable Semiconductors: Control over Carrier States and Excitations in Layered Hybrid Organic-Inorganic Perovskites. *Phy. Rev. Lett.* **2018**, *121*, 146401.

(19) Ema, K.; Inomata, M.; Kato, Y.; Kunugita, H.; Era, M. Nearly Perfect Triplet-Triplet Energy Transfer from Wannier Excitons to Naphthalene in Organic-Inorganic Hybrid Quantum-Well Materials. *Phys. Rev. Lett.* **2008**, *100*, 257401.

(20) Hu, H.; Meier, F.; Zhao, D.; Abe, Y.; Gao, Y.; Chen, B.; Salim, T.; Chia, E. E. M.; Qiao, X.; Deibel, C.; Lam, Y. M. Efficient Room-Temperature Phosphorescence from Organic–Inorganic Hybrid Perovskites by Molecular Engineering. *Adv. Mater.* **2018**, *30*, 1707621.

(21) Passarelli, J. V.; Fairfield, D. J.; Sather, N. A.; Hendricks, M. P.; Sai, H.; Stern, C. L.; Stupp, S. I. Enhanced Out-of-Plane Conductivity and Photovoltaic Performance in n = 1 Layered Perovskites through Organic Cation Design. *J. Amer. Chem. Soc.* **2018**, *140*, 7313.

(22) Gao, P.; Bin Mohd Yusoff, A. R.; Nazeeruddin, M. K. Dimensionality engineering of hybrid halide perovskite light absorbers. *Nat. Commun.* **2018**, *9*, 5028.

(23) Zhang, S.-F.; Chen, X.-K.; Ren, A.-M.; Li, H.; Bredas, J.-L. Impact of Organic Spacers on the Carrier Dynamics in 2D Hybrid Lead-Halide Perovskites. *ACS Energy Lett.,* **2018**, 17.

(24) Maheshwari, S.; Savenije, T. J.; Renaud, N.; Grozema, F. C. Computational Design of Two-Dimensional Perovskites with Functional Organic Cations. *J. Phys. Chem. C* **2018**, *122*, 17118.

(25) Yin, W.-J.; Shi, T.; Yan, Y. Unique Properties of Halide Perovskites as Possible Origins of the Superior Solar Cell Performance. *Adv. Mater.* **2014**, *26*, 4653.

(26) Fisher, G. A.; Norman, N. C. In *Adv. Inorg .Chem*; Sykes, A. G., Ed.; Academic Press: 1994; Vol. 41, p 233.

(27) Pohl, S.; Lotz, R.; Saak, W.; Haase, D. Structural Diversity in Iodoantimonates; the Anions Sb_3I, Sb_5I and Sb_6I. *Angew. Chem. Int. Ed. Engl* **1989**, *28*, 344.

(28) Lindsjö, M.; Fischer, A.; Kloo, L. Anionic Diversity in Iodobismuthate Chemistry. *Z. anorg. allg. Chem.* **2005**, *631*, 1497.

(29) Goforth, A. M.; Tershansy, M. A.; Smith, M. D.; Peterson, L.; Kelley, J. G.; DeBenedetti, W. J. I.; zur Loye, H.-C. Structural

Diversity and Thermochromic Properties of Iodobismuthate Materials Containing d-Metal Coordination Cations: Observation of a High Symmetry $[Bi_3I_{11}]^{2-}$ Anion and of Isolated I^- Anions. *J. Am. Chem. Soc.* **2011**, *133*, 603.
(30) Volonakis, G.; Haghighirad, A. A.; Milot, R. L.; Sio, W. H.; Filip, M. R.; Wenger, B.; Johnston, M. B.; Herz, L. M.; Snaith, H. J.; Giustino, F. $Cs_2InAgCl_6$: A New Lead-Free Halide Double Perovskite with Direct Band Gap. *J. Phys. Chem. Lett.* **2017**, *8*, 772.
(31) Du, K.-z.; Meng, W.; Wang, X.; Yan, Y.; Mitzi, D. B. Bandgap Engineering of Lead-Free Double Perovskite $Cs_2AgBiBr_6$ through Trivalent Metal Alloying. *Angew. Chem. Int. Ed.* **2017**, *56*, 8158.
(32) McClure, E. T.; Ball, M. R.; Windl, W.; Woodward, P. M. Cs_2AgBiX_6 (X = Br, Cl): New Visible Light Absorbing, Lead-Free Halide Perovskite Semiconductors. *Chem. Mater.* **2016**, *28*, 1348.
(33) Pantaler, M.; Cho, K. T.; Queloz, V. I. E.; García Benito, I.; Fettkenhauer, C.; Anusca, I.; Nazeeruddin, M. K.; Lupascu, D. C.; Grancini, G. Hysteresis-Free Lead-Free Double-Perovskite Solar Cells by Interface Engineering. *ACS Energy Lett.* **2018**, *3*, 1781.
(34) Slavney, A. H.; Leppert, L.; Saldivar Valdes, A.; Bartesaghi, D.; Savenije, T. J.; Neaton, J. B.; Karunadasa, H. I. Small-Band-Gap Halide Double Perovskites. *Angew. Chem. Int. Ed.* **2018**, *57*, 12765.
(35) Vargas, B.; Ramos, E.; Pérez-Gutiérrez, E.; Alonso, J. C.; Solis-Ibarra, D. A Direct Bandgap Copper–Antimony Halide Perovskite. *J. Am. Chem. Soc.* **2017**, *139*, 9116.
(36) Zhao, X.-G.; Yang, D.; Ren, J.-C.; Sun, Y.; Xiao, Z.; Zhang, L. Rational Design of Halide Double Perovskites for Optoelectronic Applications. *Joule* **2018**, *2*, 1662.
(37) Xiao, Z.; Du, K.-Z.; Meng, W.; Wang, J.; Mitzi, D. B.; Yan, Y. Intrinsic Instability of $Cs_2In(I)M(III)X_6$ (M = Bi, Sb; X = Halogen) Double Perovskites: A Combined Density Functional Theory and Experimental Study. *J. Am. Chem. Soc.* **2017**, *139*, 6054.
(38) Creutz, S. E.; Crites, E. N.; De Siena, M. C.; Gamelin, D. R. Colloidal Nanocrystals of Lead-Free Double-Perovskite (Elpasolite) Semiconductors: Synthesis and Anion Exchange To Access New Materials. *Nano Lett.* **2018**, *18*, 1118.
(39) Connor, B. A.; Leppert, L.; Smith, M. D.; Neaton, J. B.; Karunadasa, H. I. Layered Halide Double Perovskites: Dimensional Reduction of $Cs_2AgBiBr_6$. *J. Am. Chem. Soc.* **2018**, *140*, 5235.
(40) Castro-Castro, L. M.; Guloy, A. M. Organic-Based Layered Perovskites of Mixed-Valent Gold(I)/Gold(III) Iodides. *Angew. Chem. Int. Ed.* **2003**, *42*, 2771.
(41) Kojima, N.; Kitagawa, H. Optical investigation of the intervalence charge-transfer interactions in the three-dimensional gold mixed-valence compounds $Cs_2Au_2X_6$(X = Cl, Br or I). *J. Chem. Soc., Dalton Trans.* **1994**, 327.
(42) Blancon, J. C.; Stier, A. V.; Tsai, H.; Nie, W.; Stoumpos, C. C.; Traoré, B.; Pedesseau, L.; Kepenekian, M.; Katsutani, F.; Noe, G. T.; Kono, J.; Tretiak, S.; Crooker, S. A.; Katan, C.; Kanatzidis, M. G.; Crochet, J. J.; Even, J.; Mohite, A. D. Scaling law for excitons in 2D perovskite quantum wells. *Nat. Commun.* **2018**, *9*, 2254.
(43) Mitzi, D. B.; Dimitrakopoulos, C. D.; Kosbar, L. L. Structurally Tailored Organic–Inorganic Perovskites: Optical Properties and Solution-Processed Channel Materials for Thin-Film Transistors. *Chem. Mater.* **2001**, *13*, 3728.
(44) Mitzi, D. B. Organic–Inorganic Perovskites Containing Trivalent Metal Halide Layers: The Templating Influence of the Organic Cation Layer. *Inorg. Chem.* **2000**, *39*, 6107.
(45) Chaloner, P. A.; Gunatunga, S. R.; Hitchcock, P. B. Redetermination of 2,2'-bithiophene. *Acta Cryst. C,* **1994**, *50*, 1941.
(46) Zhu, X.-H.; Mercier, N.; Frère, P.; Blanchard, P.; Roncali, J.; Allain, M.; Pasquier, C.; Riou, A. Effect of Mono- versus Di-ammonium Cation of 2,2'-Bithiophene Derivatives on the Structure of Organic–Inorganic Hybrid Materials Based on Iodo Metallates. *Inorg. Chem.* **2003**, *42*, 5330.
(47) Mitzi, D. B.; Brock, P. Structure and Optical Properties of Several Organic–Inorganic Hybrids Containing Corner-Sharing Chains of Bismuth Iodide Octahedra. *Inorg. Chem.* **2001**, *40*, 2096.
(48) Jorgensen, W. L.; Severance, D. L. Aromatic-aromatic interactions: free energy profiles for the benzene dimer in water, chloroform, and liquid benzene. *J. Am. Chem. Soc.* **1990**, *112*, 4768.
(49) Oldag, T.; Aussieker, T.; Keller, H.-L.; Preitschaft, C.; Pfitzner, A. Solvothermal Synthesis and Crystal Structure Determination of $AgBiI_4$ and Ag_3BiI_6. *Z. Anorg. Allg. Chem.* **2005**, *631*, 677.
(50) Blum, V.; Gehrke, R.; Hanke, F.; Havu, P.; Havu, V.; Ren, X.; Reuter, K.; Scheffler, M. Ab initio molecular simulations with numeric atom-centered orbitals. *Comput. Phys. Commun.* **2009**, *180*, 2175.
(51) Havu, V.; Blum, V.; Havu, P.; Scheffler, M. Efficient O(N) integration for all-electron electronic structure calculation using numeric basis functions. *J. Comput. Phys.* **2009**, *228*, 8367.
(52) Xinguo, R.; Patrick, R.; Volker, B.; Jürgen, W.; Alexandre, T.; Andrea, S.; Karsten, R.; Matthias, S. Resolution-of-identity approach to Hartree–Fock, hybrid density functionals, RPA, MP2 and GW with numeric atom-centered orbital basis functions. *New J. Phys.* **2012**, *14*, 053020.
(53) Levchenko, S. V.; Ren, X.; Wieferink, J.; Johanni, R.; Rinke, P.; Blum, V.; Scheffler, M. Hybrid functionals for large periodic systems in an all-electron, numeric atom-centered basis framework. *Comput. Phys. Commun.* **2015**, *192*, 60.
(54) Knuth, F.; Carbogno, C.; Atalla, V.; Blum, V.; Scheffler, M. All-electron formalism for total energy strain derivatives and stress tensor components for numeric atom-centered orbitals. *Comput. Phys. Commun.* **2015**, *190*, 33.
(55) Perdew, J. P.; Burke, K.; Ernzerhof, M. Generalized Gradient Approximation Made Simple. *Phys. Rev. Lett.* **1996**, *77*, 3865.
(56) Tkatchenko, A.; Scheffler, M. Accurate Molecular Van Der Waals Interactions from Ground-State Electron Density and Free-Atom Reference Data. *Phys. Rev. Lett.* **2009**, *102*, 073005.
(57) Heyd, J.; Scuseria, G. E.; Ernzerhof, M. Hybrid functionals based on a screened Coulomb potential. *J. Chem. Phys.* **2003**, *118*, 8207.
(58) Heyd, J.; Scuseria, G. E.; Ernzerhof, M. Erratum: "Hybrid functionals based on a screened Coulomb potential" [J. Chem. Phys. 118, 8207 (2003)]. *J. Chem. Phys.* **2006**, *124*, 219906.
(59) Krukau, A. V.; Vydrov, O. A.; Izmaylov, A. F.; Scuseria, G. E. Influence of the exchange screening parameter on the performance of screened hybrid functionals. *J. Chem. Phys.* **2006**, *125*, 224106.
(60) Huhn, W. P.; Blum, V. One-hundred-three compound band-structure benchmark of post-self-consistent spin-orbit coupling treatments in density functional theory. *Phys. Rev. Materials* **2017**, *1*, 033803.
(61) Li, T.; Zhao, X.; Yang, D.; Du, M.-H.; Zhang, L. Intrinsic Defect Properties in Halide Double Perovskites for Optoelectronic Applications. *Phys. Rev. Applied* **2018**, *10*, 041001.
(62) Blaha, P.; Schwarz, K.; Madsen, G. K. H.; Kvasnicka, D.; Luitz, J. *WIEN2K, An Augmented Plane Wave + Local Orbitals Program for Calculating Crystal Properties*; Karlheinz Schwarz, Techn. Universität Wien, Austria: Wien, Austria, 2001.
(63) Paier, J.; Asahi, R.; Nagoya, A.; Kresse, G. Cu_2ZnSnS_4 as a potential photovoltaic material: A hybrid Hartree-Fock density functional theory study. *Phys. Rev. B* **2009**, *79*, 115126.
(64) Skone, J. H.; Govoni, M.; Galli, G. Nonempirical range-separated hybrid functionals for solids and molecules. *Phys. Rev. B* **2016**, *93*, 235106.

(65) Zhu, T.; Huhn, W. P.; Wessler, G. C.; Shin, D.; Saparov, B.; Mitzi, D. B.; Blum, V. I_2–II–IV–VI_4 (I = Cu, Ag; II = Sr, Ba; IV = Ge, Sn; VI = S, Se): Chalcogenides for Thin-Film Photovoltaics. *Chem. Mater.* **2017**, *29*, 7868.
(66) Kim, J.; Kim, H.; Chandran, M.; Lee, S.-C.; Im, S. H.; Hong, K.-H. Impacts of cation ordering on bandgap dispersion of double perovskites. *APL Mater.* **2018**, *6*, 084903.
(67) Savory, C. N.; Walsh, A.; Scanlon, D. O. Can Pb-Free Halide Double Perovskites Support High-Efficiency Solar Cells? *ACS Energy Lett.* **2016**, *1*, 949.
(68) Yang, J.; Zhang, P.; Wei, S.-H. Band Structure Engineering of $Cs_2AgBiBr_6$ Perovskite through Order–Disordered Transition: A First-Principle Study. *J. Phys. Chem. Lett.* **2018**, *9*, 31.
(69) Hoyer, M.; Hartl, H. Die Kristallstrukturen von Tl_2AgI_3 und $NaAgI_2 \cdot 3\ H_2O$. *Z. anorg. allg. Chem.* **1996**, *622*, 308.
(70) Pitzschke, D.; Curda, J.; Cakmak, G.; Jansen, M. $Ag_4I_2SeO_4$ and Ag_3ITeO_4 – Two New Silver Solid Electrolytes. *Z. anorg. allg. Chem.* **2008**, *634*, 1071.
(71) Filip, M. R.; Hillman, S.; Haghighirad, A. A.; Snaith, H. J.; Giustino, F. Band Gaps of the Lead-Free Halide Double Perovskites $Cs_2BiAgCl_6$ and $Cs_2BiAgBr_6$ from Theory and Experiment. *J. Phys. Chem. Lett.* **2016**, *7*, 2579.
(72) Even, J.; Pedesseau, L.; Jancu, J.-M.; Katan, C. Importance of Spin–Orbit Coupling in Hybrid Organic/Inorganic Perovskites for Photovoltaic Applications. *J. Phys. Chem. Lett.* **2013**, *4*, 2999.
(73) Even, J.; Pedesseau, L.; Dupertuis, M. A.; Jancu, J. M.; Katan, C. Electronic model for self-assembled hybrid organic/perovskite semiconductors: Reverse band edge electronic states ordering and spin-orbit coupling. *Phys. Rev. B* **2012**, *86*, 205301.
(74) Katan, C.; Mercier, N.; Even, J. Quantum and Dielectric Confinement Effects in Lower-Dimensional Hybrid Perovskite Semiconductors. *Chem. Rev.* **2019**, *119*, 3140.
(75) Ishihara, T.; Hirasawa, M.; Goto, T. Optical Properties and Electronic Structures of Self-Organized Quantum Well $(C_nH_{2n+1}NH_3)_2PbX_4$(X=I, Br, Cl). *Jpn. J. Appl. Phys* **1995**, *34*, 71.

Table of contents